Supplement of Solid Earth, 17, 369–387, 2026
https://doi.org/10.5194/se-17-369-2026-supplement

Solid Earth Open Access EGU

Supplement of

Unveiling tectonic deformation in El Salvador through GNSS and InSAR kinematic modelling

Juan Portela et al.

Correspondence to: Marta Béjar-Pizarro (m.bejar@csic.es)

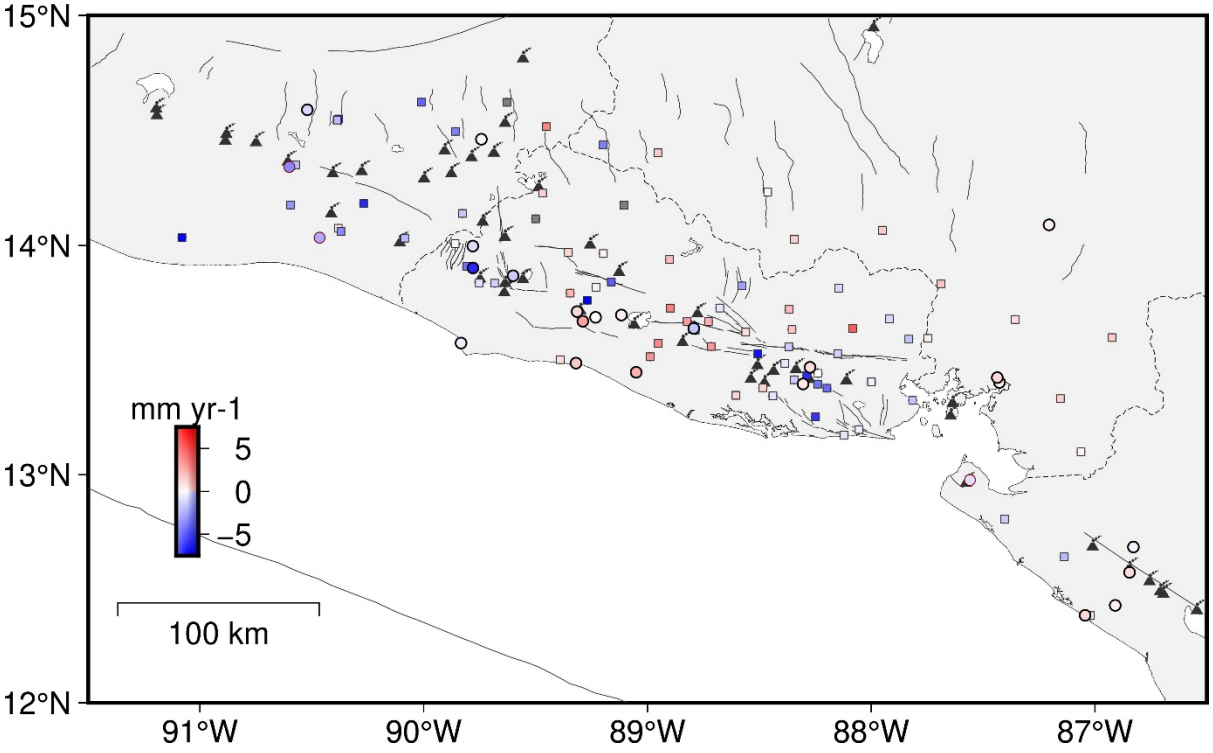

Figure S1: Vertical GNSS velocities from Portela et al. (2024), for continuous (circles) and episodic (squares) stations.

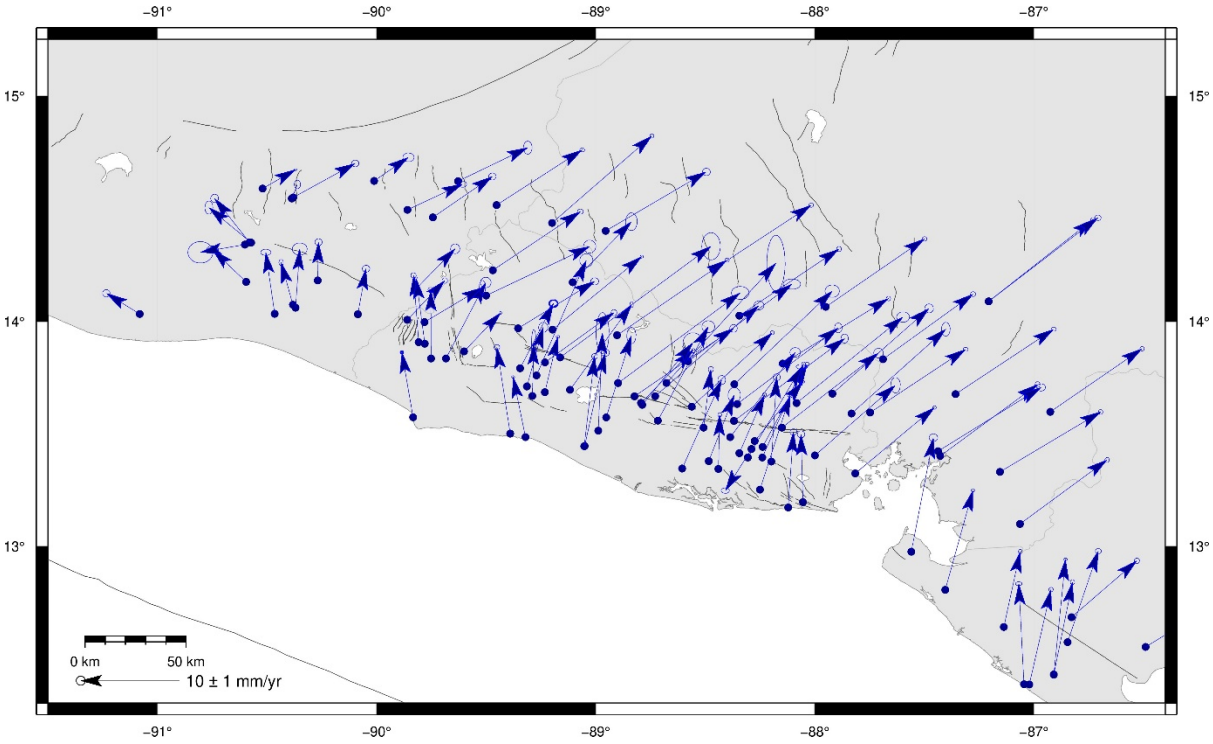

Figure S2: GNSS horizontal ITRF2014 velocities for El Salvador from Portela et al. (2024).

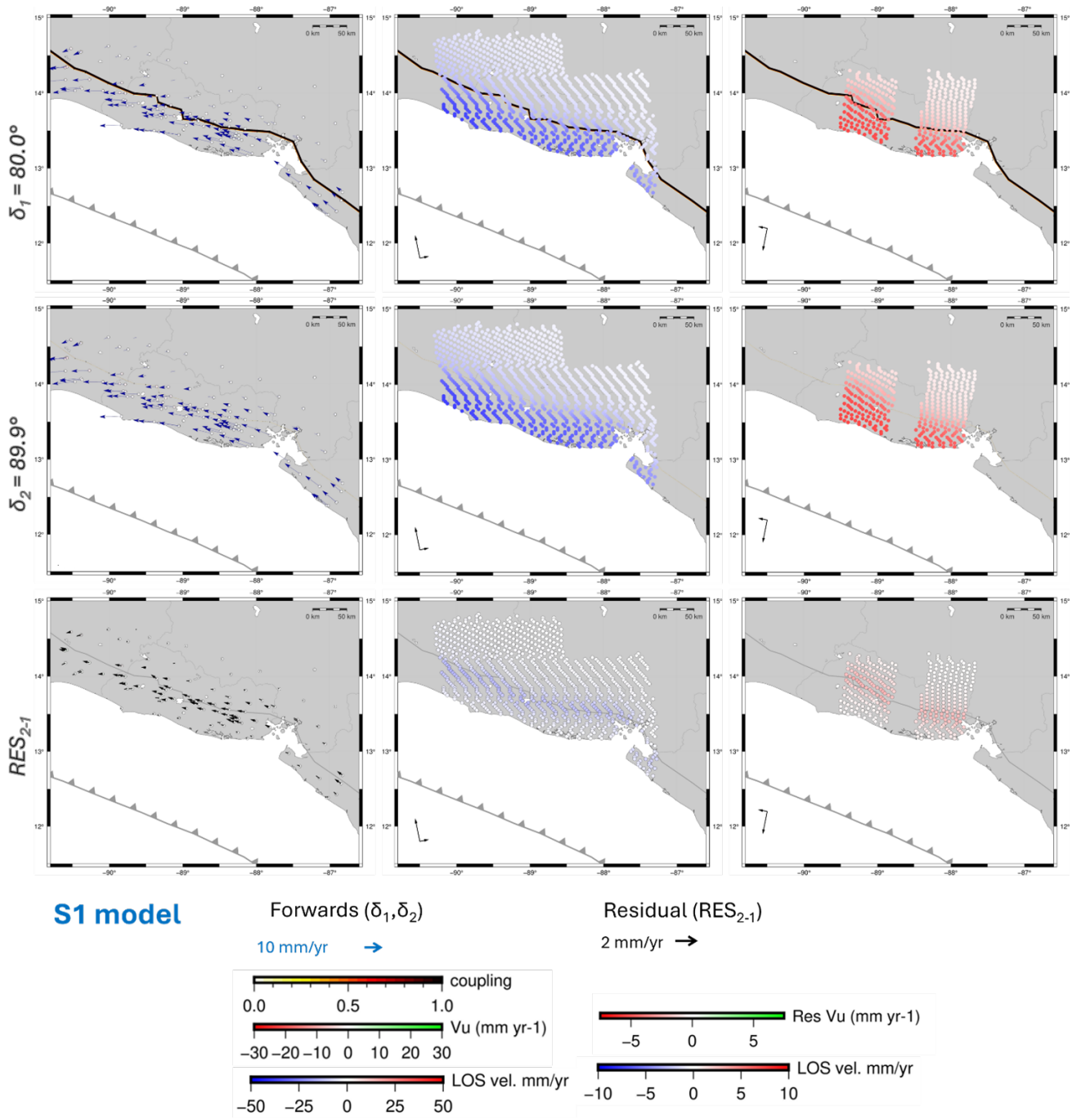

Fig. S3: Forward models (δ1 and δ2) testing the sensitivity of our models to a ~10º change in dip. GNSS velocities (left) and ALOS velocities (ascending – center, descending – right) predicted by the models are shown, along with the residuals RES2-1 between both models (last row).

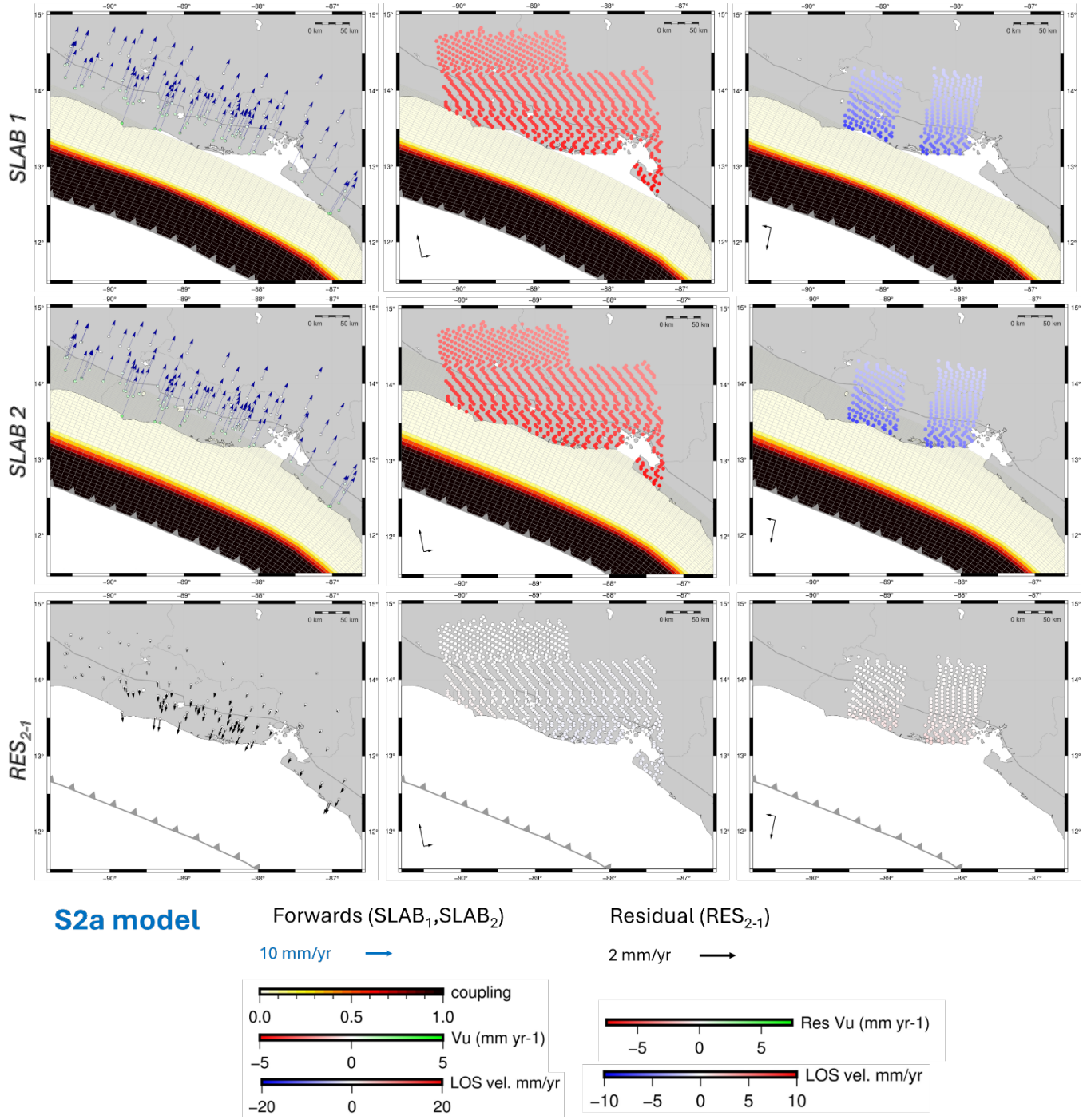

Fig. S4: Forward models (SLAB1, SLAB2) testing the sensitivity to a change in the subduction geometry, coupled in the uppermost 20 km, between Slab1 (Hayes et al., 2012) and Slab2 (Hayes et al., 2018) geometries. GNSS velocities are shown on the left (horizontal velocities as vectors and vertical velocities as color-coded circles), while ALOS velocities (ascending – center, descending – right) are displayed in the middle and right panels. The residuals between both models are shown in the last row.

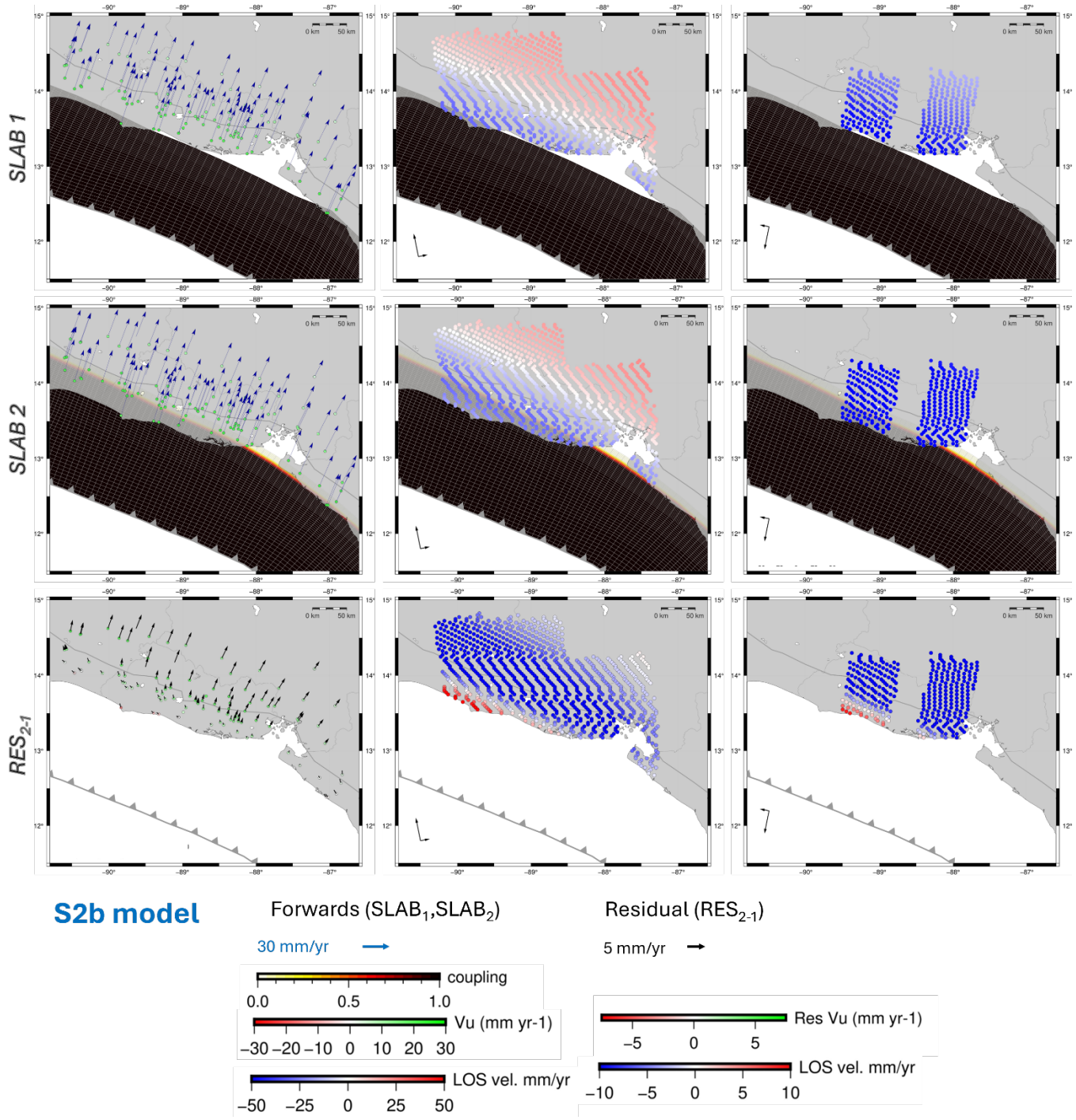

Fig. S5: Forward models (SLAB1, SLAB2) testing the sensitivity to a change in the subduction geometry, coupled in the uppermost 80 km, between Slab1 (Hayes et al., 2012) and Slab2 (Hayes et al., 2018) geometries. GNSS velocities are shown on the left (horizontal velocities as vectors and vertical velocities as color-coded circles), while ALOS velocities (ascending – center, descending – right) are displayed in the middle and right panels. The residuals between both models are shown in the last row.

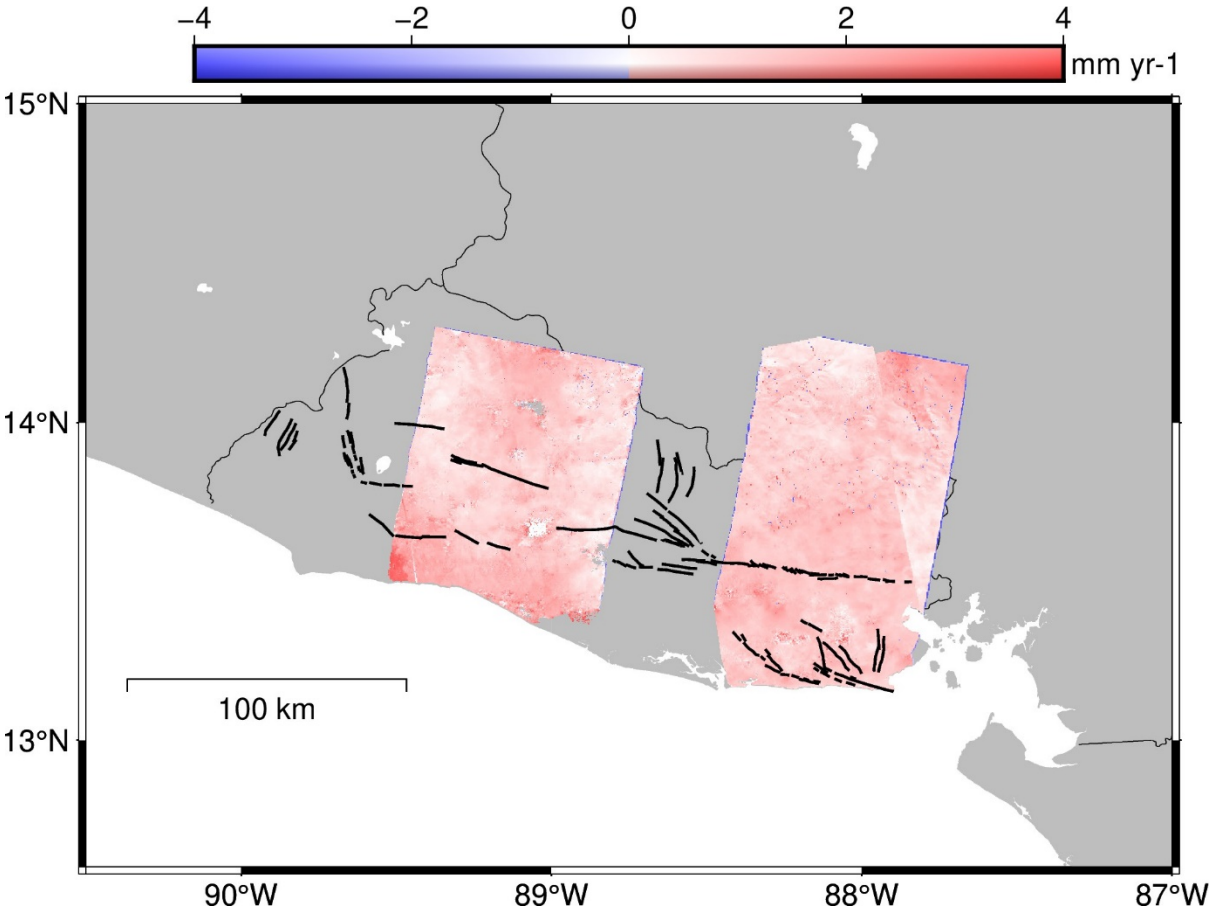

Figure S6: ALOS-derived vertical velocities, decomposed from the ascending and descending LOS velocities from Portela et al. (2024).

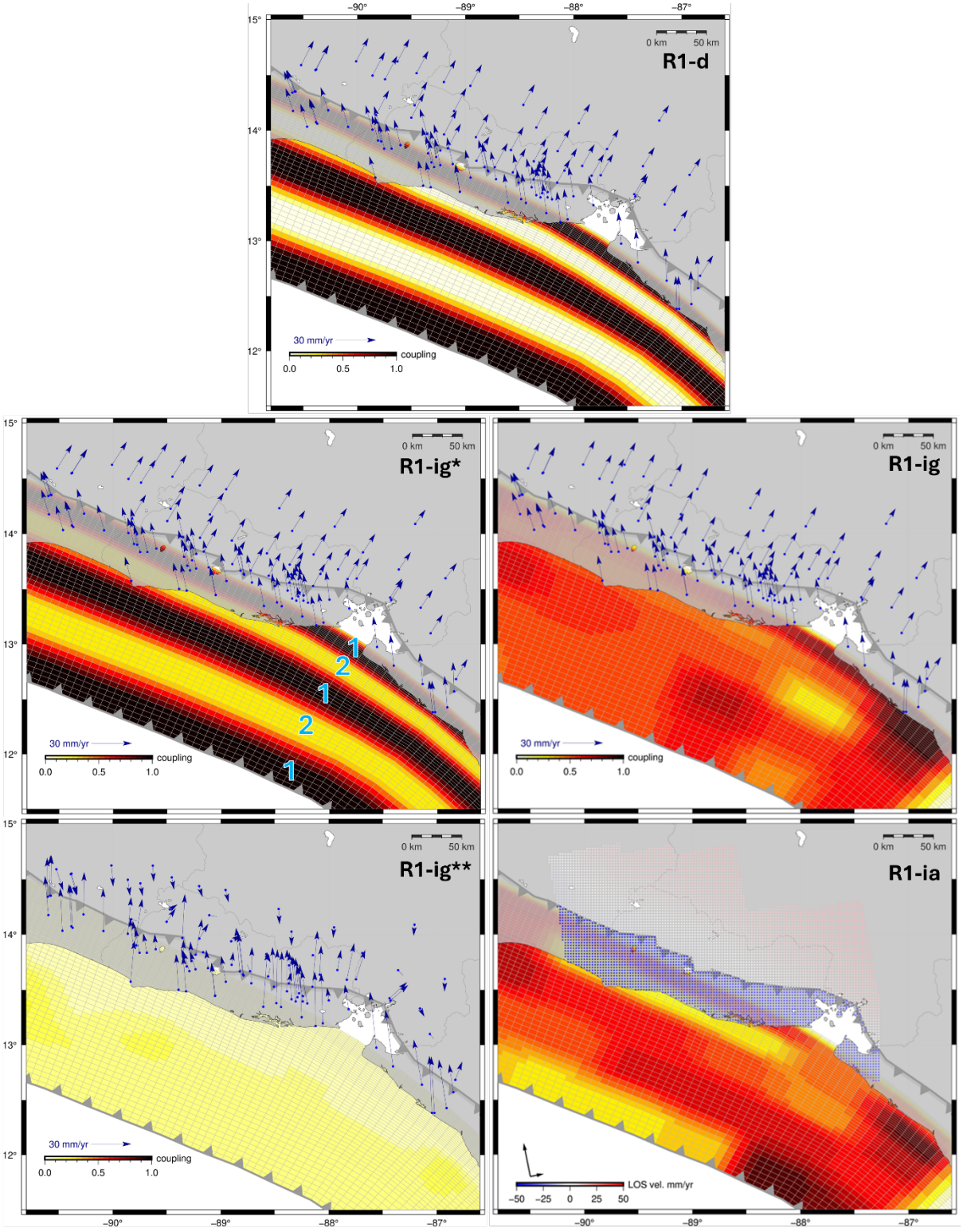

Fig. S7: Resolution model R1. The forward model (-d) and the inversions using GNSS data (-ig) and joint ALOS+GNSS data (-ia) are shown. The GNSS and ALOS velocities correspond to those calculated from the forward model (-d). The coupling pattern in panel d represents the original model, while in the other panels it corresponds to the inverted one. In this case, the GNSS data inversions are shown both with node grouping forced to match that of d (-ig*) and with all nodes left free in the inversion (-ig**).

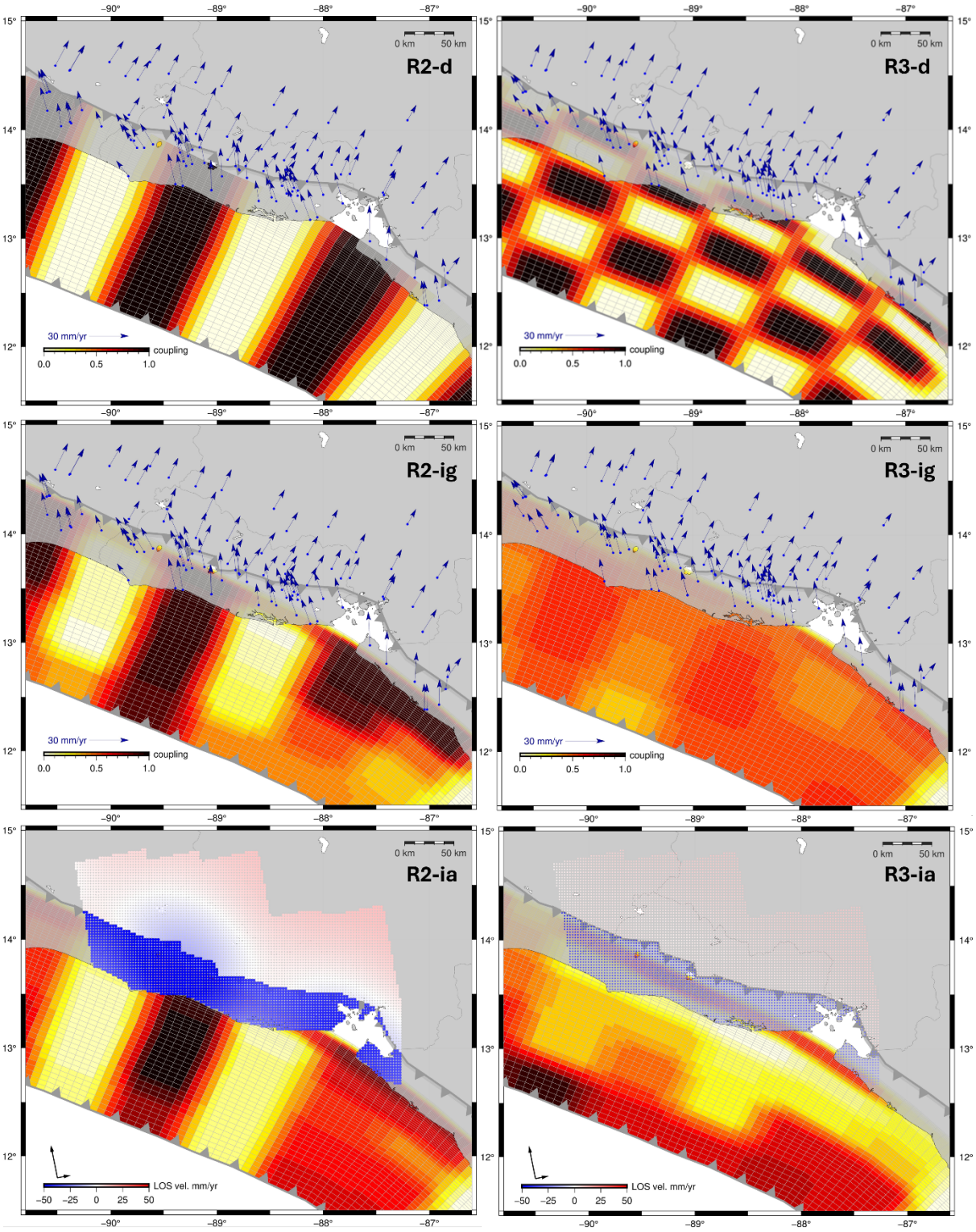

Fig. S8: Resolution models R2 and R3. The forward models (-d) and the inversions using GNSS data (-ig) and joint ALOS+GNSS data (-ia) are shown. The GNSS and ALOS velocities correspond to those calculated from the forward model (-d). The coupling pattern in panel -d represents the original model, while in the other panels it corresponds to the inverted one.

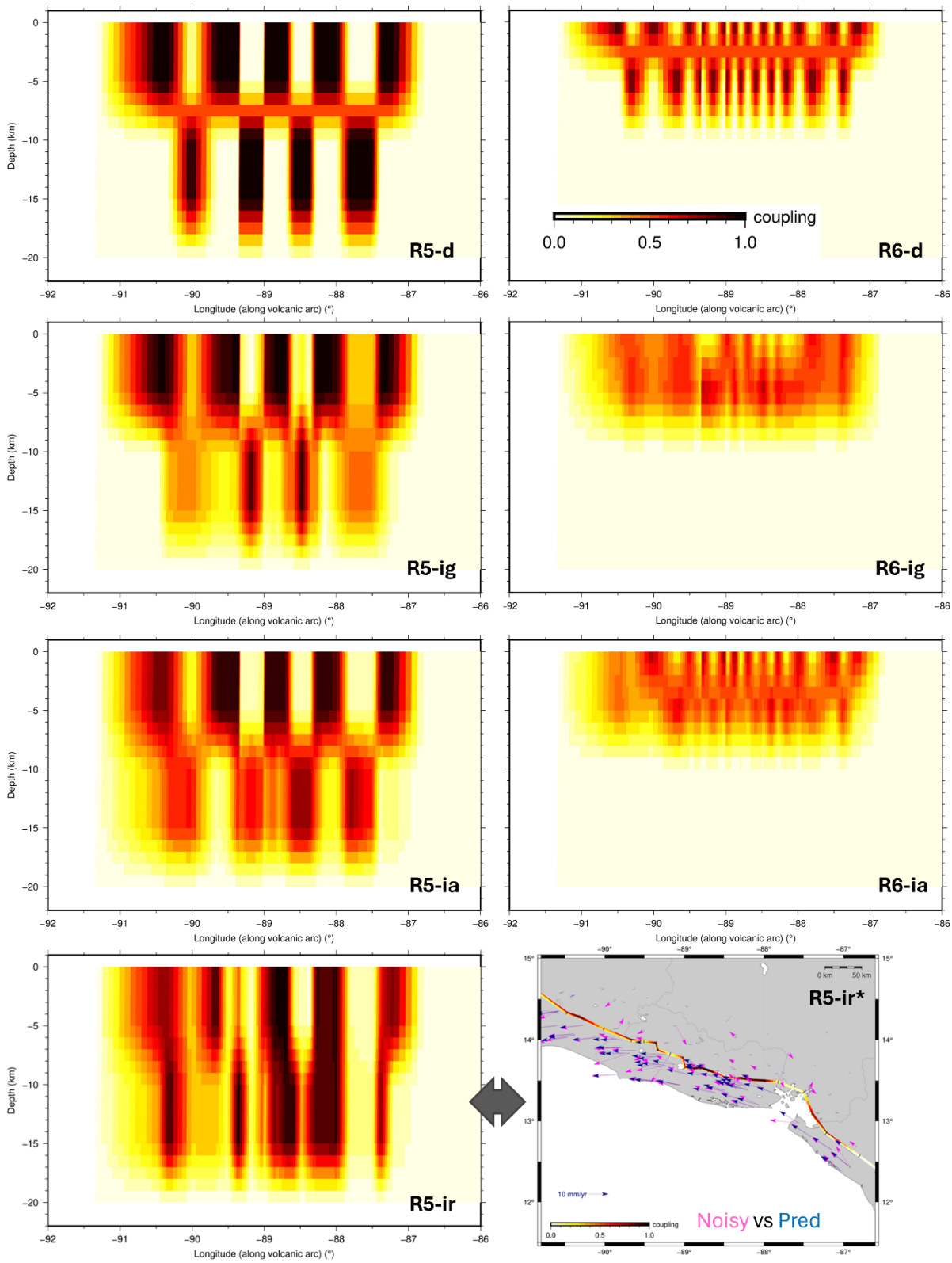

Fig. S9: Resolution models R5 and R6. The forward models (-d) and the coupling patterns obtained from the GNSS data inversions (-ig) and the joint ALOS+GNSS data inversions (-ia) are shown. The coupling pattern in panel d represents the original model, while in the other panels it corresponds to the inverted one. The inversion of the GNSS data modified with synthetic noise (R5-ir) is also shown.

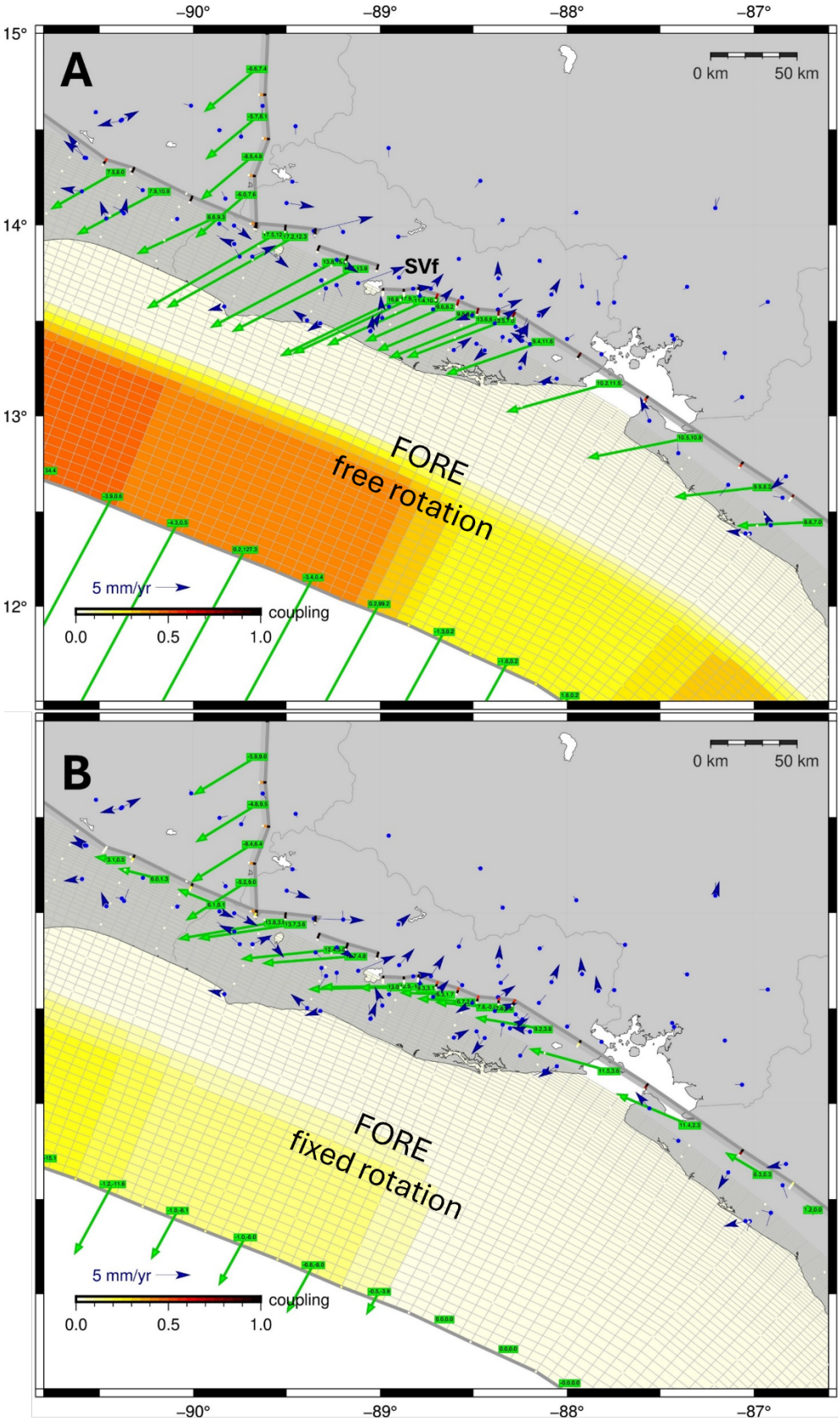

Figure S10: Inversions performed using a four-block model, allowing the ARCO block rotation pole to be free (A) and fixing it (B). Green vectors represent slip rates, while blue vectors indicate GNSS residuals.

Table S1: Compensating factor (F) for the ALOS InSAR data.

path	GNSS/path	InSARpts/path	DecInSARpts/path	F
P167	10	1177	294	5.4
P168	22	1112	278	3.6
P169	17	1565	391	4.8
P170	20	1395	349	4.2
P171	14	1263	316	4.7
P474	23	1129	282	3.5
P476	17	889	222	3.6

Table S2: Block rotations (ωx, ωy, ωz) and their uncertainties for the inverted poles of the corresponding blocks, in degrees per Million years (°/Myr), for the preferred model. Rotations without uncertainties correspond to those that remain fixed in the inversion.

BLOCK	ωx (°/Myr)	ωy (°/Myr)	ωz (°/Myr)
FORE	-0.012	-1.819	0.419
CARI	-0.046±0.002	-0.201±0.022	0.144±0.005
COCO	-0.602	-0.882	0.543
CSAL	0.02±0.014	-1.638±1.093	0.419±0.269
IPAL	0.001±0.005	-0.525±0.531	0.146±0.138
FONS	-0.035±0.026	-0.324±0.771	0.146±0.185

Table S3: Slip rate deficit (S) and uncertainties estimated in our preferred model for the main faults with consistent results. Here we include the poorly estimated fault-normal SRD (marked with an asterisk*) for the Af, Apf, Bf and Caf. The slip rates shown in brackets correspond to the model without the CSAL block.

Fault	Acronym	Fault-parallel S	Fault-normal S
Apaneca	Apf	2.9 ± 0.8	0.0 ± 0.7*
Apastepeque	Aef	3.5 ± 0.8	3.4 ± 1.6
		(8.4 ± 0.1)	(2.6 ± 0.2)
Ayagualo-Panchimalco	Af	5.5 ± 0.8	-2.7 ± 0.8*

Berlín	Bf	2.3 ± 0.8	-1.4 ± 1.6*
Comasagua	Caf	3.5 ± 0.8	-2.7 ± 0.7*
Comecayo	Cf	8.2 ± 0.8	6.8 ± 0.8
		(13.6 ± 0.1)	(4.7 ± 0.2)
Guaycume	Gf	5.6 ± 0.8	6.4 ± 0.8
		(12.4 ± 0.1)	(5.3 ± 0.2)
Ipala Graben eastern boundary	IG	-4.3 ± 0.8	9.2 ± 0.8
Jalpatagua	Jf	5.7 ± 0.6	1.7 ± 0.7
Maribios (NW)	Maf	9.4 ± 0.7	0.1 ± 1.5
Maribios (Nicaragua)	Maf	6.1 ± 0.1	0.1 ± 0.1
San Miguel	SMf	2.7 ± 0.7	0.9 ± 0.8
San Vicente	SVf	5.7 ± 0.9	2.8 ± 1.2
		(12.8 ± 0.1)	(0.9 ± 0.2)

Table S4: Number of observations (#obs), weighted root mean square error of the GNSS observations (wrms), and standard deviation of the rotation of the FONS block pole (σΩ), for each of the inversion tests performed with different geometries of the FONS block.

Test	#obs	wrms	σΩ
g51	22	1.48	1.60
g52	24	1.60	0.85
g53	8	0.49	0.66
g54	14	0.97	0.83

REFERENCES

Portela, J., Staller, A., Béjar-Pizarro, M., Hamling, I. J., and Hernández, D.: Tectonic deformation in El Salvador from combined InSAR and GNSS data, 230364, https://doi.org/10.1016/j.tecto.2024.230364, 2024.